# REPORT DOCUMENTATION PAGE

*Form Approved*
*OMB No. 0704-0188*



| **1. REPORT DATE** *(DD-MM-YYYY)* | **2. REPORT TYPE** | **3. DATES COVERED** *(From - To)* |
|---|---|---|
| March 2012 | Journal Article | March 2012- May 2012 |

**4. TITLE AND SUBTITLE**
Dynamics of Cavitation Clouds within a High-Intensity Focused Ultrasonic Beam

**5a. CONTRACT NUMBER**
In-House

**5b. GRANT NUMBER**

**5c. PROGRAM ELEMENT NUMBER**

**6. AUTHOR(S)**

Yual Lu, Joseph Katz, Andrea Prosperetti

**5d. PROJECT NUMBER**

**5e. TASK NUMBER**

**5f. WORK UNIT NUMBER**
50260542

**7. PERFORMING ORGANIZATION NAME(S) AND ADDRESS(ES)**

Air Force Research Laboratory (AFMC)
AFRL/RQRC
10 E. Saturn Blvd.
Edwards AFB CA 93524-7680

**8. PERFORMING ORGANIZATION REPORT NO.**

**9. SPONSORING / MONITORING AGENCY NAME(S) AND ADDRESS(ES)**
Air Force Research Laboratory (AFMC)
AFRL/RQR
5 Pollux Drive
Edwards AFB CA 93524-7048

**10. SPONSOR/MONITOR'S ACRONYM(S)**

**11. SPONSOR/MONITOR'S REPORT NUMBER(S)**
**AFRL-RZ-ED-JA-2012-167**

**12. DISTRIBUTION / AVAILABILITY STATEMENT**
Distribution A: Approved for Public Release; Distribution Unlimited. PA#12412

**13. SUPPLEMENTARY NOTES**
Journal Article for the Physics of Fluids Journal 2012.

**14. ABSTRACT**

In this experimental study, we generate a 500 kHz high-intensity focused ultrasonic (HIFU) beam, with pressure amplitude in the focal zone of up to 1.9 MPa, in initially quiescent water. The resulting pressure field and behavior of the cavitation bubbles are measured using high-speed digital in-line holography. Variations in the water density and refractive index field are used for determining the spatial distribution of the acoustic pressure nonintrusively. Several cavitation phenomena occur within the acoustic partial standing wave caused by the reflection of sound from the wall of the test chamber. At all sound levels, bubbly layers form in the periphery of the focal zone in the pressure nodes of the partial standing wave. At high sound levels, clouds of vapor microbubbles are generated and migrate in the direction of the acoustic beam. Both the cloud size and velocity vary periodically, with the diameter peaking in the nodes and velocity in the antinodes. A simple model involving linearized bubble dynamics, Bjerknes forces, sound attenuation by the cloud, added mass, and drag is used to predict the periodic velocity of the bubble cloud, as well as qualitatively explain the causes for the variations in the cloud size. The analysis shows that the primary Bjerknes force and drag dominate the cloud motion, and suggests that the secondary Bjerknes force causes the oscillations in the cloud size.

**15. SUBJECT TERMS**

| **16. SECURITY CLASSIFICATION OF:** | | | **17. LIMITATION OF ABSTRACT** | **18. NUMBER OF PAGES** | **19a. NAME OF RESPONSIBLE PERSON** |
|---|---|---|---|---|---|
| | | | | | Marcus Young |
| **a. REPORT** | **b. ABSTRACT** | **c. THIS PAGE** | SAR | 29 | **19b. TELEPHONE NO** *(include area code)* |
| **Unclassified** | **Unclassified** | **Unclassified** | | | 661-525-5624 |

**Standard Form 298 (Rev. 8-98)**
**Prescribed by ANSI Std. 239.18**

# Dynamics of cavitation clouds within a high-intensity focused ultrasonic beam

Yuan Lu,[1] Joseph Katz,[1,a)] and Andrea Prosperetti[1,2]

[1]*Department of Mechanical Engineering, Johns Hopkins University, Baltimore, MD 21218, USA*
[2]*Faculty of Science and Technology, Impact Institute and J. M. Burgers Center for Fluid Dynamics, University of Twente, 7500 AE Enschede, The Netherlands*

In this experimental study, we generate a 500 kHz high-intensity focused ultrasonic (HIFU) beam, with pressure amplitude in the focal zone of up to 1.9 MPa, in initially quiescent water. The resulting pressure field and behavior of the cavitation bubbles are measured using high-speed digital in-line holography. Variations in the water density and refractive index field are used for determining the spatial distribution of the acoustic pressure nonintrusively. Several cavitation phenomena occur within the acoustic partial standing wave caused by the reflection of sound from the wall of the test chamber. At all sound levels, bubbly layers form in the periphery of the focal zone in the pressure nodes of the partial standing wave. At high sound levels, clouds of vapor microbubbles are generated and migrate in the direction of the acoustic beam. Both the cloud size and velocity vary periodically, with the diameter peaking in the nodes and velocity in the antinodes. A simple model involving linearized bubble dynamics, Bjerknes forces, sound attenuation by the cloud, added mass, and drag is used to predict the periodic velocity of the bubble cloud, as well as qualitatively explain the causes for the variations in the cloud size. The analysis shows that the primary Bjerknes force and drag dominate the cloud motion, and suggests that the secondary Bjerknes force causes the oscillations in the cloud size.

## I. INTRODUCTION

High-intensity focused ultrasound (HIFU), along with the associated cavitation, is used in a variety of fields. The sonochemistry involves the use of acoustic cavitation to initiate and enhance chemical reactions.[1,2] In medical applications, extracorporeal shock wave lithotripsy induced by acoustic cavitation has been investigated extensively, both experimentally and

a) Author to whom correspondence should be addressed. Electronic mail: katz@jhu.edu.

numerically,[3,4,5,6,7] and is used in clinical practice. HIFU-induced cavitation also plays an important role in delivering drug to target cells and activating them.[8]

When bubbles are in a non-uniform acoustic field, the spatial pressure gradient coupled with their volumetric pulsation, produce a net force, which is termed the primary Bjerknes force.[9] This acoustically generated force affects the bubble trajectories along with other hydrodynamic forces such as added mass, drag, etc.[10,11] During acoustic cavitation, clouds of bubbles often form, either directly or through fission of a collapsing bubble,[12] further complicating the understanding and modeling of the dynamics involved. Relative to the single bubble cases, studies focusing on the motion of cavitation cloud in HIFU fields are relatively limited. Wu et al.[13] irradiated a cylindrical reactor with a 27.3 kHz, low level (maximum sound pressure of 100 kPa) unfocused ultrasonic beam, and observed that cavitation clouds could be generated in degassed water. The clouds traveled in the sound propagation direction toward the water-air interface at a velocity of up to 1 m/s. Willard[14] employed an intense, 2.5 MHz, focused acoustic beam, with pressure amplitude of up to 7 MPa, to study the resulting cavitation. He observed generation of plume-like bubble clouds moving at velocity of up to 10 m/s in both aerated and degassed water. The author suggested that the beam generated high-speed acoustic streaming in the liquid, which carried the clouds. He did not measure the liquid speed directly, but inferred it from the motion of microbubbles around the clouds. The measured velocity did not exceed 2 m/s, implying that other mechanisms must be involved in accelerating the clouds. The present of neighboring boundaries with the associated reflected waves further complicates the dynamics of bubble clouds.

In the present study, we generate a HIFU beam in an otherwise quiescent water container with pressure amplitude of up to 1.9 MPa, and use high-speed digital in-line holography to measure the size, spatial distribution, and velocity of the bubbles. Furthermore, holography enables us to record the spatial variations in refractive index of water subjected to the high intensity sound field, thus demonstrating a novel experimental technique to visualize and quantify the acoustic in the test tank. The phenomena we describe are complex. In order to better understand them, we develop a model involving Bjerknes forces and attenuation of the sound field by the cloud. This model is able to predict the magnitude and spatial variations in cloud velocity reasonably well.

## II. EXPERIMENTAL SETUP AND PROCEDURES

### A. Facility and Instrumentation

As illustrated in Fig. 1, the experiments have been performed in a rectangular glass tank with dimensions of 202×202×101 $mm^3$ containing tap water. The tank is open to the air on the top, and the water is initially quiescent. The HIFU transducer, manufactured by Sonic Concepts, is positioned at the center of the top of the tank, with its radiating surface immersed in water. This custom designed transducer operates at a fixed frequency $f$=500 kHz, and has a maximum input power $P_{in}$ =400 W. The corresponding wavelength $\lambda$, for a sound speed $c_0$ of 1500 m/s in water at $20\ ^{\circ}C$, is 3 mm. The transducer has a concave radiating surface with diameter $d_{rs}$ of 33 mm, which focuses the ultrasonic beam to a zone located 64 mm away from its surface. The focal zone is a cylindrical volume with a diameter $d_f$ =5.8 mm and a length of 42 mm, as provided by the manufacturer and confirmed by our measurements (see below). The 500 kHz sinusoidal signal is generated using a function generator, model No. 33220A manufactured by Agilent Technologies. The signal is amplified by a 200 W RF power amplifier, model No. 1020L, manufactured by Electronics & Innovation, and monitored using a power meter, model No. 22A, manufactured by Sonic Concepts. The signal is fed into a matching network, also manufactured by Sonic Concepts, and then into the transducer. At high power levels, the temperatures of the transducer itself and the liquid in the focal zone increase rapidly. To prevent damage to the transducer and generation of thermally induced Rayleigh–Bénard convection in the liquid, the transducer was operated in a pulse mode, each pulse lasting less than 2 seconds. The interval between two subsequent pulses was several minutes and long enough to allow the liquid to return to the quiescent condition. Every few pulses, the bubbles accumulating on the transducer's surface are removed to eliminate possible adverse effects on the ultrasonic waves.

A substantial fraction of the data acquisition about the bubble cloud characteristics as well as the sound field involves application of digital holography. Unlike conventional photography, a hologram is a record of interference of coherent light scattered from objects with a reference beam. Consequently, it not only contains information on light intensity propagating from illuminated objects, but also the phase of this light field.[15] Numerical reconstruction of the holograms at varying depths brings the objects, such as particles, bubbles, etc., into focus, enabling us to measure their size, shape and spatial distribution.[16,17,18,19,20,21] For the present

application, we employ digital in-line holography using the optical setup illustrated in Fig. 1. Due to the rapid motion of the bubble clouds (velocities of the order of m/s), the light source is a Q-switched pulsed 523 nm (green) laser, manufactured by CrystaLaser, which generates up to 0.1 mJ/pulse at a rate of up to 20 kHz. The laser beam is collimated and illuminates the volume of interest, mostly in the focal zone of the ultrasonic beam. The holograms are recorded using a high-speed CMOS camera, Photron FASTCAM-Ultima APX, which can record 2000 f/s at full resolution of 1024×1024 pixels and up to 30,000 f/s at a resolution of 256×128 pixels. The magnification varies from 1:1, for which the resolution is 17 $\mu$m/pixel, to 5:1. Numerical reconstruction is performed using in-house developed software.[15]

## B. Visualization and measurement of the HIFU pressure field

This section describes the method used to visualize the pressure field and to characterize the pressure in the focal zone of the ultrasonic beam. The pressure wave in the focal zone is nearly one-dimensional and can be expressed as

$$p\left(x,t\right)= p_0 + p'\left(x,t\right). \tag{1}$$

where $p_0$ and $p'$ are the undisturbed and acoustic pressures, respectively. The acoustic pressure can be modeled as the sum of incident $p'_{\text{in}}$ and reflected $p'_{\text{re}}$ waves

$$p'\left(x,t\right)= p'_{\text{in}}\left(x,t\right)+ p'_{\text{re}}\left(x,t\right)= p_{\text{f}}\sin\left(kx-\omega t\right)+C_{\text{R}}\,p_{\text{f}}\sin\left(kx+\omega t+\varsigma\right). \tag{2}$$

Here $k=2\pi/\lambda$ is the wave number, $\omega=2\pi f$ is the angular frequency, $p_{\text{f}}$ is the amplitude of the incident wave, and $\varsigma$ is a phase lag. To account for the attenuation of the reflected wave and the defocusing of the reflected wave, we multiply its amplitude by a reflection coefficient $C_{\text{R}}$, $0<C_{\text{R}}<1$. The magnitude of $p_{\text{f}}$ can be estimated from the input power and the efficiency ($\eta=0.85$) of the HIFU system, as provided by the manufacturer. The resulting acoustic intensity at the transducer's radiating surface is $I_{\text{rs}}=\eta P_{\text{in}}\big/\left(\pi d_{\text{rs}}^2/4\right)$, and the acoustic pressure on the surface is $p_{\text{rs}}=\left(2I_{\text{rs}}Z\right)^{1/2}$, where $Z$ is the acoustic impedance of water. The manufacturer specifies that the intensity gain in the focal zone is $g$=2.51, and the incident pressure amplitude

in the focal zone is therefore $p_f = gp_{rs}$. For example, at $P_{in} = 5$ W, $p_f = 306$ kPa, while at $P_{in} = 110$ W, $p_f = 1.44$ MPa, and at $P_{in} = 200$ W, $p_f = 1.94$ MPa.

One can also estimate the amplitude of the acoustic field from the changes to the water density. The substantial pressure fluctuations in the focal zone cause detectable variations in the density and the refractive index *n* of the water. When a collimated light beam passes through the spatially varying refractive index field, an initially collimated beam alters its direction of propagation. By placing the hologram plane (Fig. 1), namely the plane being focused on by the imaging lens, at a certain distance *H* from the center of the acoustic focal zone, the holograms contain non-uniform shadowgraphic patterns created by the angular deviations of the laser beam. A sample hologram showing the instantaneous light intensity distribution for $P_{in}$=110 W is presented in Fig. 2 (a). The instantaneous intensity fluctuation of the light field is related to the second derivative of the refractive index normal to the light axis[22]

$$\frac{I'_{z=H}}{I_0} \triangleq \frac{I_{z=H} - I_0}{I_0} = -H \int_{-df/2}^{d_f/2} \left(\nabla_\perp^2 n\right) dz, \tag{3}$$

where $I_0$ is the undisturbed intensity and $I$ is the intensity recorded at a distance $z$ from the center of the acoustic beam (see Fig. 1). Assuming that the acoustic field, and thus the density and refractive index, vary mainly in the propagation direction, $\nabla_\perp^2 n$ is reduced to $d^2n/dx^2$ and $\int_{-d_f/2}^{d_f/2} \left(\nabla_\perp^2 n\right) dz \approx \left(d^2n/dx^2\right) d_f$. For $n = n(\rho)$, $d^2n/dx^2 = (dn/d\rho)(d^2\rho/dx^2)$, where $dn/d\rho$ is a constant that can be determined from the Lorenz-Lorentz relation:[22]

$$\frac{n^2 - 1}{n^2 + 2} \frac{1}{\rho} = C, \tag{4}$$

where *C* is a constant that depends on the wavelength of the laser, properties of the liquid, temperature, and pressure. For a 523 nm laser wavelength at 20 °C and atmospheric pressure, $C = 2.1 \times 10^{-4}$ m$^3$/kg.[23] Finally, using a first order approximation, $p' = \rho' c_0^2$, the acoustic pressure can be expressed in terms of the light intensity

$$p'(x,t) = \frac{c^2}{(dn/d\rho) k^2 d_f H} \frac{I'(x,t)}{I_0}. \tag{5}$$

Given the present experimental configuration, the acoustic pressure is proportional to the light intensity passing through the focal zone, and can be estimated from the distribution of light intensity (grey level) in the holograms. The bright bands in the holograms indicate locally high pressure ( $p' > 0$ ) since the light converges, and thus brighter ( $I' > 0$ ) in regions of high refractive index [see Fig. 2 (a)].

In a partial standing wave, there are no true pressure nodes since there are no points where the rms pressure $p_{\mathrm{rms}}$ is zero. However, for convenience, we still choose to call the regions with minimum $p_{\mathrm{rms}}$ as "nodes" and those with maximum $p_{\mathrm{rms}}$ as "antinodes". For the acoustic pressure field defined in Eq. (2), $p_{\mathrm{rms}} = p_{\mathrm{f}} \left\{ 0.5 \left[ 1 + C_R^2 - 2C_R \cos\left( 2kx + \varsigma \right) \right] \right\}^{1/2}$ . The reflection coefficient can be obtained from $C_{\mathrm{R}} = \left( p_{\mathrm{rms}}^{\max} - p_{\mathrm{rms}}^{\min} \right) \Big/ \left( p_{\mathrm{rms}}^{\max} + p_{\mathrm{rms}}^{\min} \right)$. Using Eq. (5), $p_{\mathrm{rms}}$ can be replaced with the rms grey level ( $I_{\mathrm{rms}}$ ) for each pixel, i.e.

$$C_{\mathrm{R}} = \frac{I_{\mathrm{rms}}^{\max} - I_{\mathrm{rms}}^{\min}}{I_{\mathrm{rms}}^{\max} + I_{\mathrm{rms}}^{\min}}. \tag{6}$$

The distribution of $I_{\mathrm{rms}}$ for $P_{\mathrm{in}}$=110 W is shown in Fig. 2 (b), for which $I_{\mathrm{rms}}^{\max} = 21.7$ , $I_{\mathrm{rms}}^{\min} = 13.1$ , based on averaging along the central line of several antinodes and nodes, and thus $C_{\mathrm{R}} = 0.25$. Using the measured $C_{\mathrm{R}}$ , $I_{\mathrm{rms}}$, $d_{\mathrm{f}}$ provided by the manufacturer, and Eq. (5), the estimated amplitude of the incident ultrasonic wave is $p_{\mathrm{f}} = 1.32$ MPa . This result differs by about 10% from the previously mentioned amplitude calculated from information provided by the manufacturer ( $p_{\mathrm{f}} = 1.44$ MPa ). Figure 2 (b) also confirms that the width of the focal zone is consistent with the information provided by the manufacturer ( $d_{\mathrm{f}} = 5.8$ mm ).

## III. RESULTS

### A. Annular bubble structures

At all sound levels, after being generated, the bubbles grow by rectified diffusion.[24] Such gas bubbles, however, cannot survive in regions where the acoustic pressure is too high.[25] Therefore, these gas bubbles are mostly observed away from the focal zone where, under the action of the primary Bjerknes forces, they accumulate in layers separated by $\lambda / 2$. Two

examples are shown in Fig. 3, the first one showing the bubbles arranged in a vertical plane, and the second one showing a top view of the circular structure surrounding the focal zone. The resonant radius of gas bubbles at the transducer's frequency and atmospheric pressure is 5.9 $\mu$m. This radius is smaller than that of the bubbles in Fig. 3 (a) implying, based on the linear theory of the primary Bjerknes force, that the bubbles in this image are attracted to the nodes of the partial standing wave.[9] Furthermore, the secondary Bjerknes forces among bubbles are attractive.[26] Therefore, adjacent bubbles tend to move toward each other, coalesce, and form bigger bubbles. These processes are evident in the high-speed movies, and the larger bubbles in Fig. 3 (a), which vary in size between 100-250 $\mu$m, are the result of the coalescence of several small ones. The secondary Bjerknes force also causes bubbles smaller than about 20 $\mu$m to rapidly jitter and orbit around bigger ones. When the sound is turned off, these gas bubbles rise toward the free surface due to buoyancy.

## B. Cloud cavitation

At high sound levels ( $p_f \geq 1.2$ MPa ), cavitation inception occurs near the axis of the acoustic beam, not necessarily in the focal zone, and the resulting bubble clouds travel at velocities of up to 4 m/s in the direction of the incident ultrasonic wave. This velocity is several orders of magnitude larger than the acoustically induced streaming, which was measured by tracking seeded micro-particles. Two examples of superpositions of high-speed images demonstrating the formation and migration of the cloud are presented in Fig. 4. The inception of cavitation, included in Fig. 4 (b), involves explosive creation of a nearly spherical compact volume of microbubbles with size of about 200 $\mu$m, and rapid expansion of this cloud in the horizontal direction to form a migrating layer. The inception occurs over a time scale much shorter than that resolved by the currently used fastest image acquisition rate of 30,000 f/s, i.e., less than $33\,\mu$s . Even under these conditions, the velocity of the liquid surrounding the cavitation cloud remains very low, except for the regions directly affected by the cloud-induced motion, e.g. in the wake of the cloud. Thus, consistent with the observations by Willard[14], the bubble cloud motion is not induced by acoustic streaming. After a few clouds are generated, the surrounding flow field is sufficiently disturbed that the bubbly rings surrounding the focal zone shown in Fig. 3 (b) are destroyed. Turning the sound off makes the cloud disappear in less than

$33\,\mu$s, leaving no noticeable traces. This feature indicates that the bubbles in the cloud contain very little non-condensable gas, whose dissolution would take a longer time. These bubbles, therefore, contain mostly water vapor.

In general, the cloud size increases with acoustic pressure and its dynamics depends on its diameter relative to the sound wavelength. When $p_f < 1.68$ MPa, the characteristic diameter of the cloud is smaller than $\lambda/3$. In this case, the cloud expands while decelerating and contracts while accelerating periodically. The size variations are evident in Fig. 4 (a) and (b), while the changes in velocity are demonstrated in Fig. 5 using two examples. Figures 5 (a) and (b) present reconstructed holographic images of the clouds, highlighting the changes in their size and location relative to the acoustic field, clearly showing that they slow down near the nodes of the partial standing wave. Corresponding quantitative information on the cloud velocity and diameter is provided in Fig. 5 (c) and (d). Both examples confirm that the cloud velocity is minimal, and its size peaks, near the nodes. On the other hand, once formed, the thickness of the clouds fluctuates, but does not show a clear correlation with the partial standing wave structure. Increasing the magnification of the holograms enables us to resolve the spatial distribution of bubbles within the cloud. In the example presented in Fig. 6, we "collapse" a series of adjacent reconstructed planes onto a single image. The typical radius of the bubbles *r* is about 20 $\mu$m.

For $p_f \geq 1.68$ MPa, the diameter of some of the clouds becomes comparable and even larger than $\lambda/2$ [see Fig. 4 (c) and (d)]. In this case, after the initial growth phase, the cloud speed and diameter do not change significantly. As demonstrated by an unreconstructed hologram in Fig. 7, when a cloud with a diameter as large as $\lambda$ develops in the case of high sound level, the amplitude of the acoustic wave on the leeward side of the cloud is much weaker than that on its windward side. This observation indicates that there is little transmission of sound through the cloud. Furthermore, the amplitude of the wave on the acoustic windward side appears to be higher than that in the surrounding fluid, suggesting a partial reflection of the sound wave, which constructively interferes with the incident wave. These trends imply that, by preventing sound transmission, the partial standing wave is eliminated and, with it, the periodic variations in the cloud's size and velocity vanish. To confirm this statement, we covered the bottom of the test chamber with fiber bristles in order to attenuate the sound reflection. Indeed, irrespective of incident sound level, the periodic variations in cloud's velocity and size

disappeared, supporting our hypothesis that both of them are caused by the partial standing wave. In the following sections, we develop a model that explains the periodic behavior of the bubble clouds.

## IV. A MODEL FOR THE AXIAL MOTION OF THE BUBBLE CLOUD

The cloud resembles a pancake-like mixture of vapor and water, with volume of $V = \pi R^2 S$, where $R$ and $S$ are its radius and thickness, respectively. However, some of its features are more easily estimated by approximating it as a sphere with an equivalent radius of $R_e = (3S/4R)^{1/3} R$. The velocity of the cloud is three orders of magnitude lower than the speed of sound in water, i.e. the associated time scales are very different. Consequently, it is reasonable to perform an analysis of the cloud dynamics, averaging over many acoustic cycles, but allowing time to vary on the cloud's time scale. The force balance on the cloud is

$$\bar{F}_{\mathrm{PB}} + \bar{F}_{\mathrm{Att}} + \bar{F}_{\mathrm{D}} + \bar{F}_{\mathrm{AM}} = \bar{\rho}_{\mathrm{m}} \bar{V} \ddot{x}, \tag{7}$$

where the overbar denotes time averaging, dot denotes time derivative with respect to the cloud time scale, $\bar{F}_{\mathrm{PB}}$ is the primary Bjerknes force, $\bar{F}_{\mathrm{Att}}$ is the propulsive force due to sound attenuation in the cloud, $\bar{F}_{\mathrm{D}}$ is the drag, $\bar{F}_{\mathrm{AM}}$ is the added mass, $\bar{\rho}_{\mathrm{m}} = \left(1-\bar{\varphi}\right)\bar{\rho} + \bar{\varphi}\,\bar{\rho}_{\mathrm{V}} \approx \left(1-\bar{\varphi}\right)\bar{\rho}$ is the density of the bubbly mixture, $\bar{\varphi}$ is the time averaged vapor volume fraction, and $\bar{\rho}$ and $\bar{\rho}_{\mathrm{V}}$ are the time averaged densities of water and vapor, respectively. For the present measurements, $\bar{\varphi}$ is about 1%. For such a volume fraction, the buoyancy force is two orders of magnitude smaller than the other contributions and, consequently, it is neglected. Note that the buoyancy force also acts in the opposite direction to the cloud motion. With expressions for all the forces, we obtain a second order ordinary differential equation for the cloud displacement, and then solve it numerically.

The primary Bjerknes force on a cloud is (see, e.g., Ref. [9])

$$\bar{F}_{\mathrm{PB}} = -\overline{V' \partial_x p'}, \tag{8}$$

where the apostrophe denotes the oscillatory part of the relevant quantities. For simplicity, we assume small oscillations of the cloud size, and estimate $V'$ by using a spherical model, in which $R_e'$ is calculated from the linearized Rayleigh-Plesset equation[27]

$$\ddot{R}_e' + 2\beta\dot{R}_e' + \Omega_r^2 R_e' = -\frac{p'}{\bar{\rho}\bar{R}_e}, \tag{9}$$

where $\beta$ and $\Omega_r$ are the damping coefficient and resonant frequency of the cloud, respectively, and are functions of $x$. Substituting the pressure fluctuations associated with the partial standing wave [Eq. (2)], we obtain

$$\begin{aligned} R_e' = &-\frac{p_f}{\bar{\rho}\bar{R}_e\omega^2\left\{\left[\left(\frac{\Omega_r}{\omega}\right)^2-1\right]^2+4\left(\frac{\beta}{\omega}\right)^2\right\}} \\ &\times\left\{\left[\left(\frac{\Omega_r}{\omega}\right)^2-1\right]\left[\sin\left(kx-\omega t\right)+C_R\sin\left(kx+\omega t+\varsigma\right)\right]+2\left(\frac{\beta}{\omega}\right)\left[\cos\left(kx-\omega t\right)-C_R\cos\left(kx+\omega t+\varsigma\right)\right]\right\}. \end{aligned} \tag{10}$$

With $V' \approx 4\pi\bar{R}_e^2 R_e'$, the primary Bjerknes force (8) becomes

$$\bar{F}_{PB} = \frac{4\pi k\bar{R}_e p_f^2}{\bar{\rho}\omega^2\left\{\left[\left(\frac{\Omega_r}{\omega}\right)^2-1\right]^2+4\left(\frac{\beta}{\omega}\right)^2\right\}}\left\{C_R\left[\left(\frac{\Omega_r}{\omega}\right)^2-1\right]\sin\left(2kx+\varsigma\right)+\left(1-C_R^2\right)\frac{\beta}{\omega}\right\}. \tag{11}$$

The first term in this expression is associated with the standing wave, and oscillates with a spatial period of $\lambda/2$. Since $\Omega_r < \omega$, as shown below, this contribution is always directed toward the pressure nodes. The second term corresponds to the propagating part of the wave due to the partial reflection of the incident wave. This part of the force always points in the direction of the incident wave.

To obtain $\Omega_r$ for the cloud, we use the result of a linear analysis, which shows that a spherical bubble cloud has a series of resonance frequencies[28]

$$\Omega_j = \omega_r \Bigg/ \left[1+\frac{3\bar{\varphi}\left(1-\bar{\varphi}\right)}{\left(j-1/2\right)^2\pi^2}\left(\frac{\bar{R}_e}{\bar{r}}\right)^2\right]^{1/2}, \tag{12}$$

where $j$=1, 2, 3,…, $\omega_r$ is the resonant frequency of an individual bubble, and $\overline{r}$ is its mean radius, which is 20 $\mu$m for the present measurements. Although this equation was originally developed for clouds consisting of gas bubbles, it can readily be shown that it is applicable for the case of vapor bubbles, provided that $\omega_r$ is the natural frequency of a single vapor bubble. Since the lowest mode is dominant,[28] we will use $\Omega_r = \Omega_1$. Note that $\Omega_r$ is always smaller than $\omega_r$.

The damping coefficient $\beta$ can be estimated by relating the cloud's properties to those of the individual bubbles through the compressibility of the mixture $K_m = \left(\rho_m c_m^2\right)^{-1} \approx \left[\left(1-\overline{\varphi}\right)\overline{\rho} c_m^2\right]^{-1}$, where $c_m$ is the speed of sound within the cloud. By definition, $K_m = -\left(1/V\right)\left(dV/dp\right) \approx -\left(3/\overline{R}_e\right)\left(dR_e'/dp'\right)$, and $dR_e'/dp'$ can be obtained from the solution to Eq. (9), $R_e' = -p' \Big/ \left\{\overline{\rho}\overline{R}_e\omega^2\left[\left(\frac{\Omega_r}{\omega}\right)^2 - 1 + i2\left(\frac{\beta}{\omega}\right)\right]\right\}$, where $i=\sqrt{-1}$. By taking the real part [denoted with $\Re\{\ \}$] of $dR_e'/dp'$, we have

$$K_m = -\frac{3}{\overline{R}_e}\Re\left\{\frac{dR_e'}{dp'}\right\} = \frac{3\left[\left(\frac{\Omega_r}{\omega}\right)^2 - 1\right]}{\overline{\rho}\overline{R}_e^2\omega^2\left\{\left[\left(\frac{\Omega_r}{\omega}\right)^2 - 1\right]^2 + 4\left(\frac{\beta}{\omega}\right)^2\right\}}. \tag{13}$$

The complex sound speed in a bubbly mixture containing either gas or vapor bubbles is given by[29]

$$\frac{1}{c_m^2} = \frac{1}{c_0^2} + \frac{3\overline{\varphi}}{\overline{r}^2\omega^2\left[\left(\frac{\omega_r}{\omega}\right)^2 - 1 + i2\left(\frac{b}{\omega}\right)\right]}, \tag{14}$$

where $b$ is the damping coefficient of an individual bubble. Since $\left(1-\overline{\varphi}\right)\overline{\rho}K_m \approx \Re\left\{1/c_m^2\right\}$,

$$\beta = \frac{\omega}{2}\left\{\frac{3\left(1-\overline{\varphi}\right)\left(\frac{\overline{r}}{\overline{R}_e}\right)^2}{\left(\frac{\overline{r}\omega}{c_0}\right)^2 \Big/ \left[\left(\frac{\Omega_r}{\omega}\right)^2 - 1\right] + 3\overline{\varphi} \Big/ \left(\left[\left(\frac{\omega_r}{\omega}\right)^2 - 1\right]^2 + 4\left(\frac{b}{\omega}\right)^2\right)} - \left[\left(\frac{\Omega_r}{\omega}\right)^2 - 1\right]^2\right\}^{1/2}. \tag{15}$$

The expressions of $\omega_{\mathrm{r}}$ and $b$ of a linearly oscillating vapor bubble are provided in Ref. [30]:

$$\omega_{\mathrm{r}}=\left[\frac{1}{\overline{\rho}\overline{r}^{2}}\left(3\frac{\Re\{K\}-B\Im\{K\}}{|K|^{2}}-\frac{2\sigma}{\overline{r}}\right)\right]^{1/2}, \tag{16}$$

and

$$b=\frac{3}{2\omega\overline{\rho}\overline{r}^{2}}\frac{\Im\{K\}+B\Re\{K\}}{|K|^{2}}, \tag{17}$$

where $\Im\{\ \}$ denotes the imaginary part, $\sigma$ is the surface tension, $K$ is the complex compressibility of a vapor bubble

$$\begin{aligned}K=&\frac{1}{\gamma\overline{p}_{\mathrm{b}}}\\&+3\frac{c_{\mathrm{s}}}{L}\left(\frac{\gamma-1}{\gamma}\frac{\overline{T}_{\mathrm{s}}}{\overline{p}_{\mathrm{b}}}-\frac{dT_{\mathrm{s}}}{dp}\right)\left[\frac{D_{\mathrm{v}}}{i\omega\overline{r}^{2}}-\sqrt{\frac{D_{\mathrm{v}}}{i\omega\overline{r}^{2}}}\coth\left(\sqrt{\frac{i\omega\overline{r}^{2}}{D_{\mathrm{v}}}}\right)\right]\\&-\frac{i3\kappa_{\mathrm{w}}}{\overline{\rho}_{\mathrm{v}}L\omega\overline{r}^{2}}\left(1+\sqrt{\frac{i\omega\overline{r}^{2}}{D_{\mathrm{w}}}}\right)\frac{dT_{\mathrm{s}}}{dp},\end{aligned} \tag{18}$$

$$B=\frac{2\kappa_{\mathrm{w}}}{\overline{\rho}_{\mathrm{v}}LD_{\mathrm{w}}}\frac{dT_{\mathrm{s}}}{dp}\frac{2D_{\mathrm{w}}}{\omega\overline{r}^{2}}\left(p_{0}-\overline{p}_{\mathrm{V}}+\frac{2\sigma}{\overline{r}}\right)\left[1-3G\left(\sqrt{\frac{\omega\overline{r}^{2}}{2D_{\mathrm{w}}}}\right)\right], \tag{19}$$

and

$$G(w)=w^{4}\int_{0}^{\infty}\frac{\exp\left[-(1+i)s\right]}{(w+s)^{5}}ds. \tag{20}$$

In the expressions above, $\gamma$ is the ratio of the specific heats, $c_{\mathrm{s}}$ is the specific heat of the vapor along the saturation line, $L$ is the latent heat, $\overline{T}_{\mathrm{s}}$ is the mean temperature at the vapor-water interface, $\overline{p}_{\mathrm{b}}$ is the mean pressure in the bubble, $dT_{\mathrm{s}}/dp\approx\overline{T}_{\mathrm{s}}/(L\overline{\rho}_{\mathrm{V}})$, $D_{\mathrm{v}}$ and $D_{\mathrm{w}}$ are the thermal diffusivity of vapor and water, respectively, $\kappa_{\mathrm{w}}$ is the thermal conductivity of water, and $\Delta p$ is the difference between the liquid static pressure and the saturation pressure. For the

current case, $2D_{\mathrm{W}}/\left(\omega\bar{r}\right)^2 = 2.2\times10^{-4}$, which is much smaller than unity. As a result, $B$ is negligible and the calculation can be greatly simplified.[30,31] Using the current parameters, $\omega_{\mathrm{r}} = 0.12\omega$ and $b = 0.072\omega$, and as a result $\Omega_{\mathrm{r}}$ [Eq. (12)] is at least an order of magnitude smaller than $\omega$. All the terms needed for calculating $\beta$ [Eq. (15)] and $\bar{F}_{\mathrm{PB}}$ [Eq. (11)] are now available.

Next, we estimate the propulsive force due to sound attenuation in the cloud, $\bar{F}_{\mathrm{Att}}$. The attenuation of the acoustic momentum flux (or the Reynolds stress) in the cloud[29,32] results in a net radiation force aimed in the sound propagation direction

$$\bar{F}_{\mathrm{Att}} = \pi\bar{R}^2\bar{\rho}\Delta\overline{u'^2}. \tag{21}$$

Here $u'$ is the acoustically induced liquid velocity and $\Delta$ denotes the difference across the cloud. For a linear acoustic wave, the velocity fluctuation on the acoustic windward side of the cloud is $u'_{\mathrm{wind}} = \left[\, p'_{\mathrm{in}} - p'_{\mathrm{re}}\exp\left(-\alpha S\right)\right]/\left(\bar{\rho}c_0\right)$, and on the leeward side is $u'_{\mathrm{lee}} = \left[\, p'_{\mathrm{in}}\exp\left(-\alpha S\right) - p'_{\mathrm{re}}\right]/\left(\bar{\rho}c_0\right)$, where $\alpha$ is the attenuation coefficient across the cloud. In this estimate, we assume that the cloud is small enough that the local sound diffraction by it does not affect the overall strength of the reflected wave. Substituting Eq. (2) for the pressure, and time averaging, we obtain

$$\bar{F}_{\mathrm{Att}} = \frac{\left(1-e^{-2\alpha\bar{S}}\right)\left(1-C_{\mathrm{R}}^2\right)p_{\mathrm{f}}^2\pi\bar{R}^2}{2\bar{\rho}c_0^2}. \tag{22}$$

The attenuation coefficient is calculated from the complex sound speed in a bubbly mixture[29]

$$\alpha = -\omega\Im\left\{\frac{1}{c_{\mathrm{m}}}\right\} \tag{23}$$

Using Eq. (14), and the present conditions, we obtain $\alpha = 8.47\times10^3$ 1/m and $\exp\left(-2\alpha\bar{S}\right) = 0.034$ for a characteristic cloud thickness of $200\,\mu$m, i.e., the wave is substantially attenuated across the cloud.

The drag force on the cloud is

$$\overline{F}_{\mathrm{D}} = -\tfrac{1}{2} C_{\mathrm{D}} \overline{\rho} \pi \overline{R}^2 \dot{x}^2, \tag{24}$$

where $C_{\mathrm{D}}$ is the drag coefficient. For a wide range of Reynolds numbers, the drag coefficient of a circular disk is essentially unity.[33] Finally, for the added mass, we estimate it assuming a spherical cloud with an equivalent radius,

$$\overline{F}_{\mathrm{AM}} = -\overline{m}_{\mathrm{add}} \ddot{x} = -\tfrac{2}{3} \overline{\rho} \pi \overline{R}_{\mathrm{e}}^3 \ddot{x}. \tag{25}$$

Using the derived expressions for the forces, and a change of variables to $X = x + \frac{\varsigma}{2k}$ in order to eliminate the irrelevant phase lag $\varsigma$, we obtain the following nonlinear second order differential equation

$$\begin{aligned} \ddot{X} = & -\frac{C_{\mathrm{D}}}{2\left(1.5-\overline{\varphi}\right)\overline{S}} \dot{X}^2 \\ & + \frac{4kp_{\mathrm{f}}^2 \overline{R}_{\mathrm{e}}}{\left(1.5-\overline{\varphi}\right)\overline{\rho}^2 \omega^2 \overline{R}^2 \overline{S}} \frac{C_{\mathrm{R}}\left[\left(\frac{\Omega_{\mathrm{r}}}{\omega}\right)^2 - 1\right]\sin X + \left(1-C_{\mathrm{R}}^2\right)\beta/\omega}{\left\{\left[\left(\frac{\Omega_{\mathrm{r}}}{\omega}\right)^2 - 1\right]^2 + 4\left(\frac{\beta}{\omega}\right)^2\right\}} \\ & + \frac{\left(1-\mathrm{e}^{-2\alpha\overline{S}}\right)\left(1-C_{\mathrm{R}}^2\right)p_{\mathrm{f}}^2}{2\left(1.5-\overline{\varphi}\right)\overline{\rho}^2 c_0^2 \overline{S}}. \end{aligned} \tag{26}$$

To solve this equation, we need the dimensions of the cloud whose characteristics are discussed briefly in the following section, along with its void fraction. To estimate the cloud motion, we use the experimental observation that $\overline{R}(X)$ oscillates nearly harmonically in space and, as a result, we estimate it as $\overline{R}(X) = 0.5\left[\left(\overline{R}_{\max} - \overline{R}_{\min}\right)\cos 2kX + \left(\overline{R}_{\max} + \overline{R}_{\min}\right)\right]$. Based on the average dimensions of 30 clouds, we use $\overline{R}_{\max} = 350\ \mu\mathrm{m}$ and $\overline{R}_{\min} = 100\ \mu\mathrm{m}$ as the characteristic maximum and minimum radius, respectively. The thickness does not show a clear correlation with the partial standing wave, and seems to fluctuate about some mean value. For the calculation, we use the average thickness of the 30 clouds, $\overline{S} = 200\ \mu\mathrm{m}$. With the initial conditions $X(0) = \lambda/4$, $\dot{X}(0) = 0$, since cavitation inception typically occurs in the pressure antinodes, Eq. (26) is solved using the Matlab solver "ode45". Figure 8 (a) shows the "steady-state" solution for $p_{\mathrm{f}} = 1.44$ MPa, and compares it to the measured cloud velocity averaged

over 30 clouds. The model reproduces the correct magnitude of cloud velocity, but there is a phase difference. In the case of a big cloud ( $\bar{R} = 1.5$ mm, $p_f = 1.89$ MPa ), for which $C_R = 0$, the model predicts a constant steady-state velocity of 1.36 m/s (after the initial acceleration), which is 12% lower than the averaged observed value (1.54 m/s).

Figure 8 (b) shows the variations of calculated forces normalized using the predicted mean velocity and characteristic mean radius. In the vicinity of the nodes the total force is negative, and thus decelerating the cloud there. The primary Bjerknes force and the drag contribute to this deceleration, while the attenuation force and added mass are positive. Although the latter are small, without the attenuation and added mass, the cloud would not have enough inertia to escape from the nodes, and would be trapped there. Near the antinodes, the primary Bjerknes force propels the cloud.

## V. MECHANISMS AFFECTING THE BUBBLE CLOUD SIZE

In the previous section, the measured variations in cloud size were used as an input. In this section, we discuss possible mechanisms affecting the periodic contraction and expansion of the smaller cloud. As mentioned before, the radius of such clouds peaks at the pressure nodes and is minimal at the antinodes. Since the cloud rapidly disappears when the sound is turned off, the bubbles much contain mostly vapor with gas diffusion playing a minor role. Also, the pressure oscillations at the antinodes are higher than those at the nodes, implying that the larger cloud at the node cannot be caused by excessive cavitation there. A possible mechanism involves interactions among bubbles, such as the secondary Bjerknes force,[26] namely the force on a bubble resulting from the pressure field generated by volume oscillations of all the other bubbles in a cloud.

It is well known that the secondary Bjerknes force between two equal bubbles, according to linear theory, is attractive both when the bubbles are driven above and below the resonance frequency. The theory gives this force in the form[26]

$$\bar{F}_{SB} = -\frac{\bar{\rho}}{4\pi \bar{l}^2} \overline{\dot{v}_1' \dot{v}_2'}, \tag{27}$$

where $v_1'$ and $v_2'$ are the oscillating bubble volumes, and $l$ is the distance between the bubbles. To estimate this force, we assume that the two bubbles have the same equilibrium radius, which

is larger than the resonant size, and that they are subjected to the pressure expressed in Eq. (2). Solving the linearized Rayleigh-Plesset equation[27] for each bubble to estimate the volume oscillations gives

$$\bar{F}_{\mathrm{SB}} = -\frac{2\pi \bar{r}^2 p_{\mathrm{f}}^2}{\bar{\rho}\omega^2 \bar{l}^2 \left( \left[ \left( \frac{\omega_{\mathrm{r}}}{\omega} \right)^2 - 1 \right]^2 + 4\left( \frac{b}{\omega} \right)^2 \right)} \left( -2C_{\mathrm{R}} \cos X + C_{\mathrm{R}}^2 + 1 \right). \tag{28}$$

As is evident, $\bar{F}_{\mathrm{SB}}$ is negative, i.e., it is an attractive force.[26] However, its magnitude peaks at the antinodes, where the pressure oscillation peaks, and is minimal at the nodes. Thus, the bubbles within the cloud are more likely to form dense clusters in the vicinity of the antinodes. The magnitude of the secondary Bjerknes force can be of the same order as the primary Bjerknes force, especially when many bubbles are involved. Thus, the influence of $\bar{F}_{\mathrm{SB}}$ is not negligible, and its variations along the path of the cloud could cause the changes to the cloud volume observed during experiments.

## SUMMARY AND CONCLUSIONS

In this study, we have used high-speed digital in-line holography to observe and measure cavitation phenomena within a high intensity focused ultrasonic beam in otherwise quiescent water. The amplitude of pressure oscillations is sufficiently high to cause corresponding changes to the water density and, consequently, to its refractive index. These changes are recorded in holograms and used to estimate the amplitude of pressure oscillations. The partially attenuated wave reflected by the container walls interference with the primary wave giving rise to a partial standing wave, in which the pressure field consists of both traveling and standing components with clearly defined pressure nodal and antinodal regions. Clouds of cavitation bubbles typically appear first near the antinodes, and then travel at speeds of several m/s in the same direction as the primary sound wave, consistent with prior observations.[13,14] The typical cloud size is a fraction of a millimeter, much smaller than the ultrasonic beam size, and it contains hundreds of microbubbles with typical radius of 20 $\mu$m. Since the bubbles disappear in less then our fastest frame rate of 33 $\mu$s, we conclude that they contain mostly vapor. Therefore, the diffusion of non-condensable gases dissolved in the liquid does not play a significant role. The size and speed of the smaller clouds vary periodically, with the speed peaking at the nodes,

and the size at the antinodes. When the cloud becomes large enough to block a significant fraction of the acoustic beam, these variations disappear. Under such conditions, after an initial growth, the cloud size and 1-2 m/s propagation velocity remain approximately constant.

The cloud motion cannot be a result of acoustic streaming since the bubbles are transported at speeds that are much higher than that of the liquid surrounding the cloud. To explain the observed phenomena, we have used a model that accounts for the primary Bjerknes force, sound attenuation, added mass and drag. The volumetric oscillation of the cloud, required for calculating the primary Bjerknes force, as well as the sound attenuation through the cloud, are estimated using linearized theories. With the cloud size as an input, the model predicts fairly well the velocity magnitude and its variations along the partial standing wave. The dominant forces in the cloud dynamics are the primary Bjerknes force and the drag force. The model also predicts the cloud motion when the sound attenuation is high enough to eliminate the reflected wave.

The oscillations in cloud size, which peaks in the nodal regions, cannot be caused by spatial variations in cavitation, since the pressure oscillations peak at the antinodes. To explain them, at least qualitatively, we consider the effect of the secondary Bjerknes force, which involves the interaction among bubbles. The force calculated using linear bubble dynamics indicates attraction among the bubbles, which increases with the magnitude of pressure oscillations and can be of the same order as the primary Bjerknes force. This attraction would reduce the cloud size around the antinodes to a greater extent than in the vicinity of the nodes, possibly explaining the observed trends.

## ACKNOWLEDGEMENTS

The authors would also like to thank Yuri Ronzhes for his contributions to the construction of the experimental setups.

## REFERENCES

[1]K. S. Suslick, Y. Didenko, M. M. Fang, T. Hyeon, K. Kolbeck, W. B. MacNamara III, M. M. Mdleleni, and M. Wong, "Acoustic cavitation and its chemical consequences," Phil. Trans. R. Soc. Lond. A. **357**, 335-353 (1999).

[2]K. S. Suslick, "Sonochemistry," Science **247**, 1439–1445 (1990).

[3]L. A. Crum, "Cavitation microjets as a contributory mechanism for renal calculi disintegration in ESWL," J. Urol. **140**, 1587-1590 (1988).

[4]J. J. Rassweiler, T. Knoll, K.-U. Köhrmann, J. a McAteer, J. E. Lingeman, R. O. Cleveland, M. R. Bailey, and C. Chaussy, "Shock wave technology and application: an update," European urology **59**, 784-96 (2011).

[5]J. Krimmel and T. Colonius, "Numerical simulation of shock wave generation and focusing in shockwave lithotripsy," J. Acoust. Soc. Am 3327 (2008).

[6]O. A. Sapozhnikov, A. D. Maxwell, B. MacConaghy, and M. R. Bailey, "A mechanistic analysis of stone fracture in lithotripsy," J. Acoust. Soc. Am **121**, 1190-1202 (2007).

[7]Y. Matsumoto, J. S. Allen, S. Yoshizawa, T. Ikeda, and Y. Kaneko, "Medical ultrasound with microbubbles," Experimental Thermal and Fluid Science **29**, 255-265 (2005).

[8]C. C. Coussios and R. a. Roy, "Applications of Acoustics and Cavitation to Noninvasive Therapy and Drug Delivery," Annual Review of Fluid Mechanics **40**, 395-420 (2008).

[9]T. G. Leighton, A. J. Walton, and M. J. W. Pickworth, "Primary bjerknes forces," European Journal of Physics **11**, 47-50 (1990).

[10]J. Rensen, D. Bosman, J. Magnaudet, C.-D. Ohl, A. Prosperetti, R. Tögel, M. Versluis, and D. Lohse, "Spiraling Bubbles: How Acoustic and Hydrodynamic Forces Compete," Physical Review Letters **86**, 4819-4822 (2001).

[11]A. Doinikov, "Translational motion of a spherical bubble in an acoustic standing wave of high intensity," Physics of Fluids **14**, 1420 (2002).

[12]C. E. Brennen, "Fission of collapsing cavitation bubbles," Journal of Fluid Mechanics **472**, 153-166 (2002).

[13]C. Wu, N. Nakagawa, and Y. Sekiguchi, "Observation of multibubble phenomena in an ultrasonic reactor," Experimental Thermal and Fluid Science **31**, 1083-1089 (2007).

[14]G. W. Willard, "Ultrasonically Induced Cavitation in Water: A Step-by-Step Process," The Journal of the Acoustical Society of America **25**, 669 (1953).

[15]J. Katz and J. Sheng, "Applications of Holography in Fluid Mechanics and Particle Dynamics," Annual Review of Fluid Mechanics **42**, 531-555 (2010).

[16]J. H. Milgram, "Computational reconstruction of images from holograms," Applied optics **41**, 853-64 (2002).

[17]J. Sheng, E. Malkiel, and J. Katz, "Digital holographic microscope for measuring three-dimensional particle distributions and motions.," Applied optics **45**, 3893-901 (2006).

[18]Y. Lu, B. Gopalan, E. Celik, J. Katz, and D. M. Van Wie, "Stretching of turbulent eddies generates cavitation near a stagnation point," Physics of Fluids **22**, 041702 (2010).

[19]F. Dubois, L. Joannes, and J.-C. Legros, "Improved Three-Dimensional Imaging with a Digital Holography Microscope With a Source of Partial Spatial Coherence," Applied Optics **38**, 7085-7094 (1999).

[20]U. Schnars and W. Jüptner, "Direct recording of holograms by a CCD target and numerical reconstruction.," Applied Optics **33**, 179-181 (1994).

[21]W. Xu, M. H. Jericho, I. a Meinertzhagen, and H. J. Kreuzer, "Digital in-line holography for biological applications.," Proceedings of the National Academy of Sciences of the United States of America **98**, 11301-5 (2001).

[22]R. J. Goldstein, *Fluid mechanics measurements* (Taylor & Francis, Philadelphia, 1996 ).

[23]I. Thormählen, J. Straub, and U. Grigull, "Refractive index of water and its dependence on wavelength, temperature, and density," J. Phys. Chem. **14**, 933-945 (1985).

[24]C. E. Brennen, *Fundamentals of multiphase flow* (Cambridge University Press, New York, 2005 ).

[25]M. P. Brenner, S. Hilgenfeldt, and D. Lohse, "Single-bubble sonoluminescence," Reviews of Modern Physics **74**, 425-484 (2002).

[26]L. A. Crum, "Bjerknes forces on bubbles in a stationary sound field," The Journal of the Acoustical Society of America **57**, 1363-1370 (1975).

[27]M. S. Plesset and A. Prosperetti, "Bubble dynamics and cavitation," Annual Review of Fluid Mechanics **9**, 145-185 (1977).

[28]L. D'Agostino and C. E. Brennen, "Linearized dynamics of spherical bubble clouds," J. Fluid Mech **199**, 155–176 (1989).

[29]K. W. Commander and A. Prosperetti, "Linear pressure waves in bubbly liquids: Comparison between theory and experiments," J. Acoust. Soc. Am **85**, 732–746 (1989).

[30]Y. Hao and A. Prosperetti, "The dynamics of vapor bubbles in acoustic pressure fields," Physics of fluids **11**, 2008 (1999).

[31]V. N. Alekseev, "Steady-state behavior of a vapor bubble in an ultrasonic field," Sov. Phys. Acoust. **21**, 311 (1976).

[32]L. D'Agostino and C. E. Brennen, "Acoustical absorption and scattering cross sections of spherical bubble clouds," Journal of the Acoustical **84**, 2126-2134 (1988).

[33]F. W. Roos and W. W. Willmarth, "Some experimental results on sphere and disk drag," AIAA Journal **9**, 285–291 (1971).

## FIGURES AND CAPTIONS

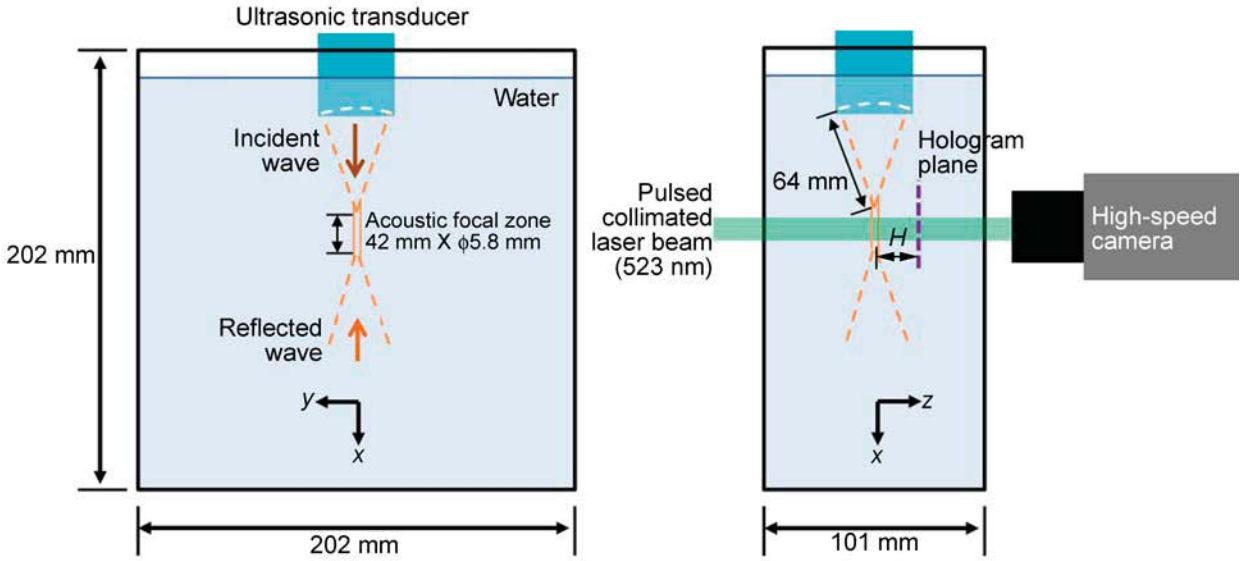


Fig. 1. (Color online) Setups for the acoustic cavitation and high-speed digital in-line holography measurements.

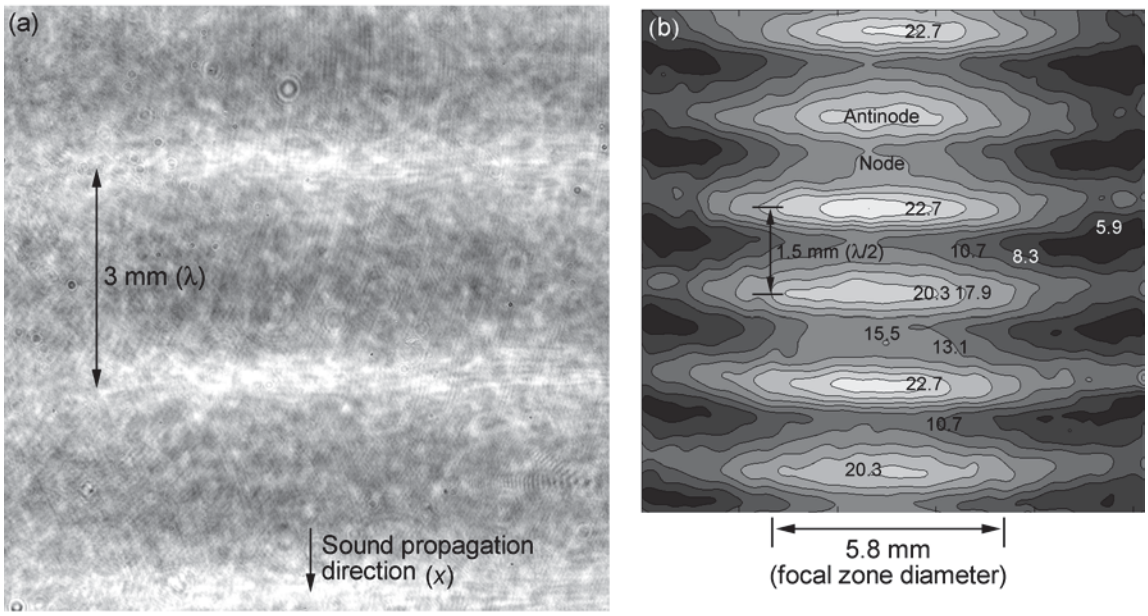


Fig. 2. Visualization and quantification of the focal zone of the ultrasonic wave; $p_f$=1.44 MPa. (a) A sample hologram showing the instantaneous acoustic wave. The bright bands correspond to high pressure. (b) The distribution of the rms grey levels, showing the partial standing wave structure.

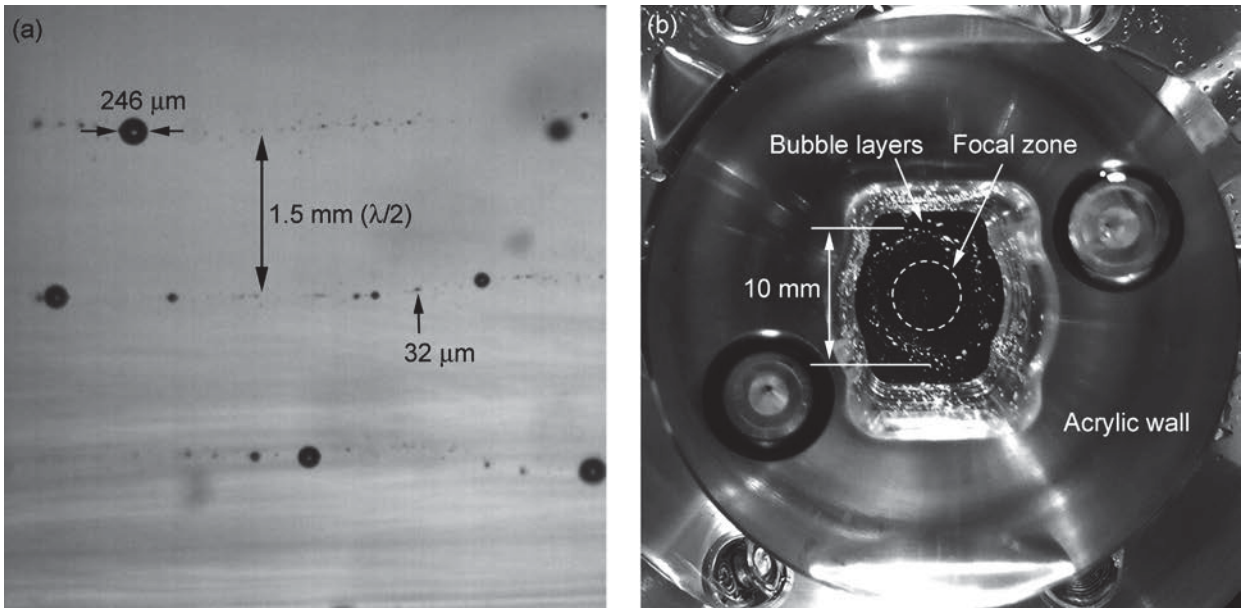


Fig. 3. (a) Annular bubble layers in the pressure nodes at low sound intensity ($p_f$=306 kPa) recorded using white light illumination. (b) A top-view of an early test chamber showing that the bubbles accumulate in the periphery of the focal zone (denoted with dashed circle).

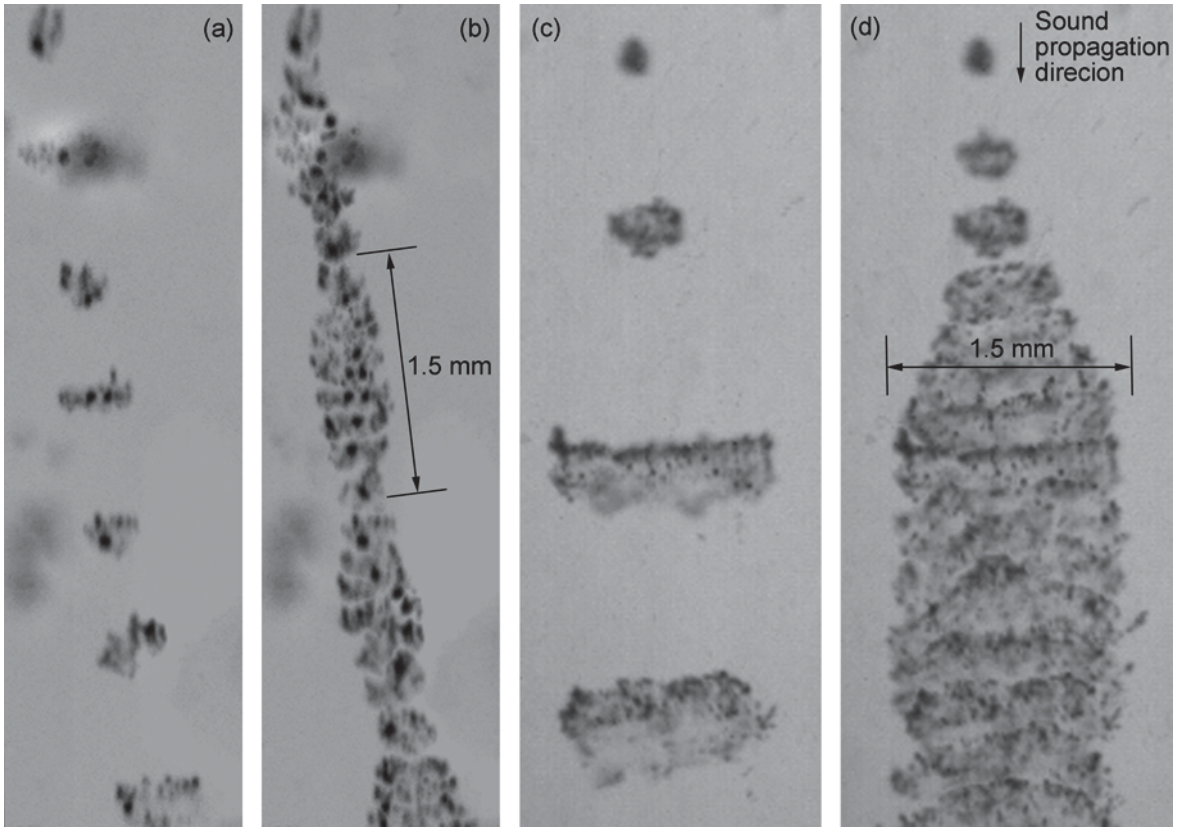


Fig. 4. Superpositions of time series of sample bubble clouds recorded using white light at (a-b) high sound level ($p_f$=1.44 MPa), where the speed and diameter of the cloud are periodic, with (a) showing a few samples and (b) containing the entire series; (c-d) very high sound level ($p_f$=1.89 MPa), where the cloud becomes large, travels at almost a constant velocity, and maintains constant diameter after the initial growth phase. Here (c) shows a few samples and (d) the entire series.

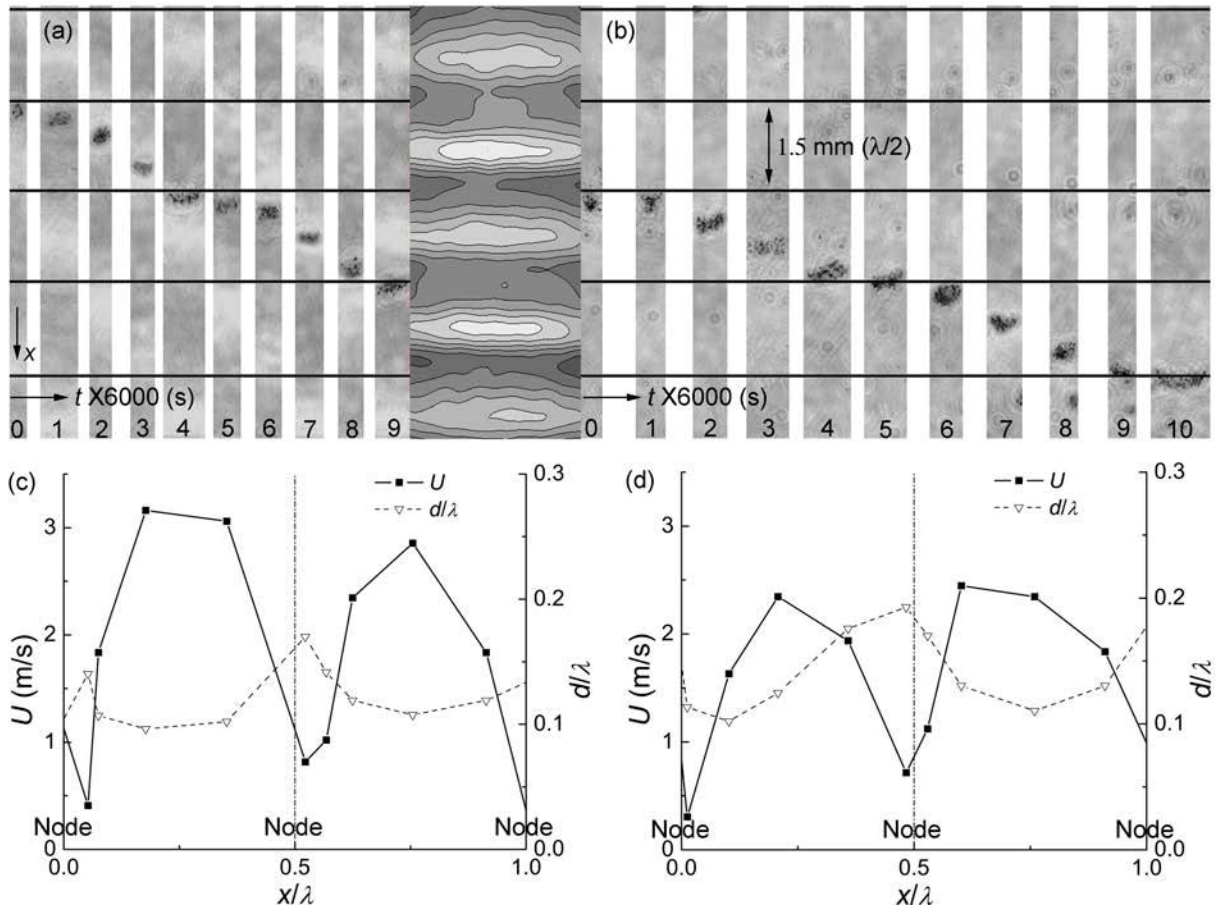


Fig. 5. (a-b) Time series of reconstructed holograms ($\Delta t$=167 $\mu$s) showing the axial locations of two sample bubble clouds in a motion cycle, and the corresponding location of the pressure nodes (thick solid-lines) determined from the distribution of rms pressure levels; $p_f$=1.44 MPa. (c-d) Corresponding velocity and diameter *vs.* the cloud location in a motion cycle.

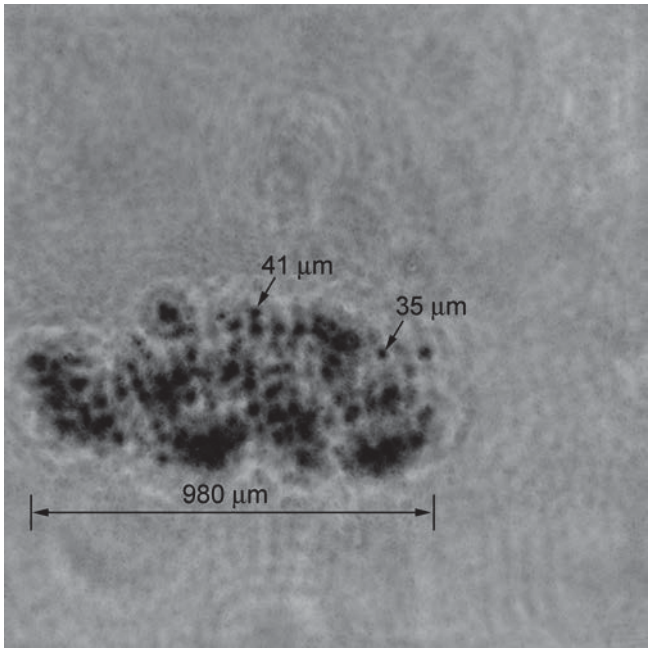


Fig 6. A close-up view of the inner structure of a bubble cloud; $p_f$=1.44 MPa. This picture is generated by collapsing a series of reconstructed holograms from different depths onto a single plane.

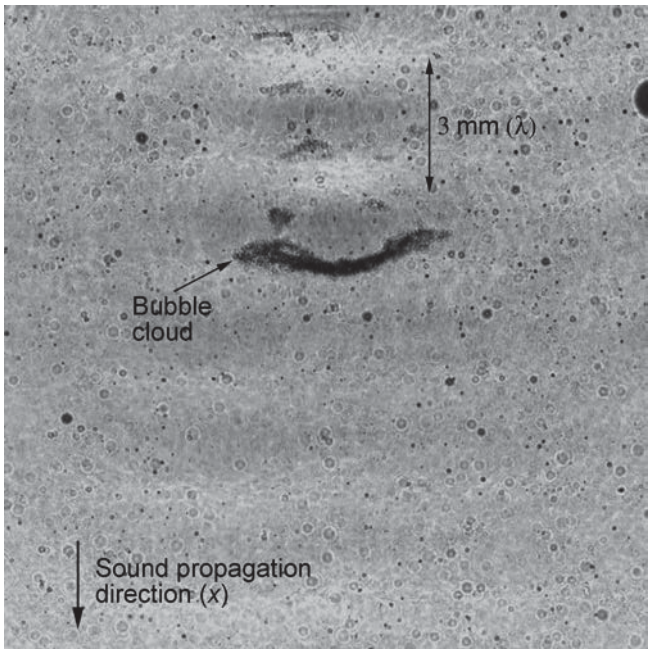


Fig. 7. A sample original instantaneous hologram showing the reflection of the incident acoustic wave by a large bubble cloud; $p_t$=1.89 MPa. The wave on the leeward side of the cloud becomes nearly invisible. The bubbles that are out of focus can be seen in the background.

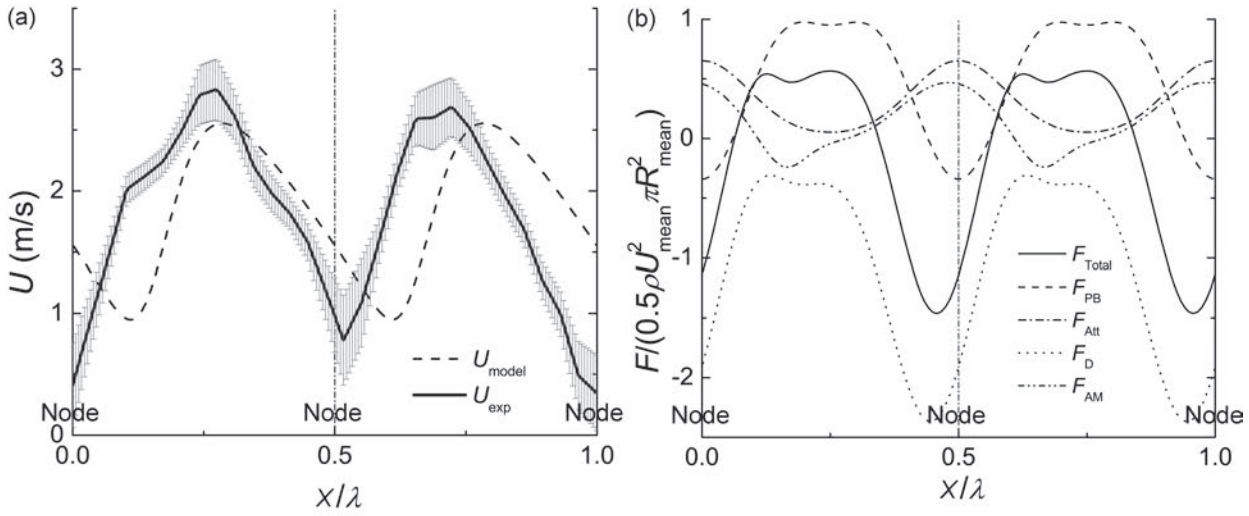


Fig. 8. (a) A comparison between the measured and predicted [Eq. (26**)**] bubble cloud velocity. The error bars indicate the standard deviation of the measured values. (b) The predicted total force and its components; $p_f$=1.44 MPa.